Circular Fringe Projection Method for 3D Profiling of High Dynamic Range Objects

Jagadeesh Kumar Mandapalli[1], Sai Siva Gorthi[2], Ramakrishna Sai Gorthi[1] and Subrahmanyam Gorthi[1]

[1]*Department of Electrical Engineering, Indian Institute of Technology, Tirupati, Andhra Pradesh, 517506, India*

[2]*Department of Instrumentation and Applied Physics, Indian Institute of Science, Bangalore, 560012, India*

Keywords: 3D Shape Measurement, Fourier Transform, Fringe Projection, High Dynamic Range.

Abstract: Fringe projection profilometry is a widely used active optical method for 3D profiling of real-world objects. Linear fringes with sinusoidal intensity variations along the lateral direction are the most commonly used structured pattern in fringe projection profilometry. The structured pattern, when projected onto the object of interest gets deformed in terms of phase modulation by the object height profile. The deformed fringes are demodulated using methods like Fourier transform profilometry for obtaining the wrapped phase information, and the unwrapped phase provides the 3D profile of the object. One of the key challenges with the conventional linear fringe Fourier transform profilometry (LFFTP) is that the dynamic range of the object height that can be measured with them is very limited.

In this paper we propose a novel circular fringe Fourier transform profilometry (CFFTP) method that uses circular fringes with sinusoidal intensity variations along the radial direction as the structured pattern. A new Fourier transform-based algorithm for circular fringes is also proposed for obtaining the height information from the deformed fringes. We demonstrate that, compared to the conventional LFFTP, the proposed CFFTP based structure assessment enables 3D profiling even at low carrier frequencies, and at relatively much higher dynamic ranges. The reasons for increased dynamic range with circular fringes stem from the non-uniform sampling and narrow band spectrum properties of CFFTP. Simulation results demonstrating the superiority of CFFTP over LFFTP are also presented.

1 INTRODUCTION

3D shape reconstruction techniques are widely used in various fields like industrial automation, computer vision, and medical imaging. Among the available methods, fringe projection technique is a commonly used active optical method (Gorthi and Rastogi, 2010) for 3D profiling because of its righteous properties like non-contact based non-destructive operation and its ability to give high resolution. Furthermore, with the fringe projection technique, the 3D shape of an object can be reconstructed from a single image, and thus it can be used for real time 3D shape measurements.

Fig. 1 shows a typical experimental set-up used in fringe projection technique. A structured pattern, usually linear fringes with sinusoidal intensity variation along the lateral direction, is projected onto the object of interest. The projected pattern gets phase modulated in accordance with the object height profile (or depth profile), and it is recorded with a camera. The recorded pattern is phase-demodulated and the result is unwrapped for obtaining the actual height of the object at each pixel location.

Several methods have been developed in the literature for phase demodulation, e.g., Fourier transform profilometry (Takeda and Mutoh, 1983; Lin and Su, 1995; Su and Chen, 2001), windowed Fourier transform profilometry (Kemao, 2004; Kemao, 2007), spatial phase detection method (Toyooka and Iwaasa, 1986; Sajan et al., 1998), and wavelet transform method (Dursun et al., 2004; Zhong and Weng, 2004; Gdeisat et al., 2006). Since phase demodulation methods result in wrapped phase whose values are mapped to the range $[-\pi, \pi)$, these are generally followed by a phase unwrapping procedure. Phase unwrapping is performed using methods like ZπM (Dias and Leitão, 2002), Goldstein's phase unwrapping (Goldstein et al., 1988), branch cut (Gutmann and Weber, 2000), flood fill (Asundi and Wensen, 1998), region

Mandapalli, J., Gorthi, S., Gorthi, R. and Gorthi, S.
Circular Fringe Projection Method for 3D Profiling of High Dynamic Range Objects.
DOI: 10.5220/0007389608490856
In *Proceedings of the 14th International Joint Conference on Computer Vision, Imaging and Computer Graphics Theory and Applications (VISIGRAPP 2019)*, pages 849-856
ISBN: 978-989-758-354-4

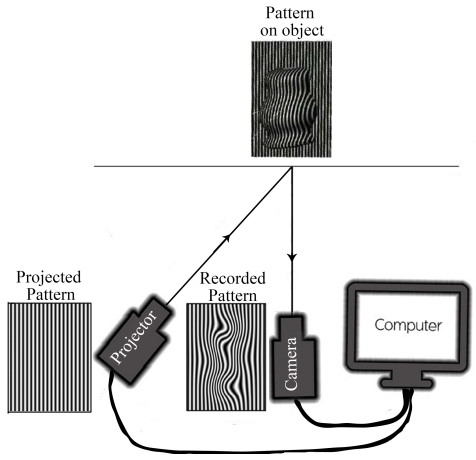

Figure 1: Schematic diagram illustrating the principle of fringe projection profilometry. Structured pattern generated in the computer is projected onto the object (lying on reference plane) through the projector and the phase modulated pattern is captured through the camera for further analysis.

growing phase unwrapping (Baldi, 2003), regularized phase tracking (Servin et al., 1999), and multilevel quality guided phase unwrapping algorithm (Zhang et al., 2007). It can be noted that the aforementioned phase-demodulation algorithms are applicable only for linear fringes.

Various types of structured patterns have been proposed in the literature for fringe projection profilometry. Typically, the intensity profiles of these structured patterns are repetitive along the lateral direction. Linear fringes having sinusoidal intensity profile along the lateral direction are the most commonly used fringe pattern (Gorthi and Rastogi, 2010). Other types of patterns include hexagonal grating (Iwata et al., 2008), linear fringes with triangular intensity profile (Jia et al., 2008) and sawtooth intensity profile (Chen et al., 2005) along the lateral direction.

In this paper, we propose a novel circular fringe-based profilometry that employs circular fringes with sinusoidal intensity variations along the radial direction as the structured pattern. We also propose a new approach for quantifying the underlying phase of the radially varying circular fringes. Unlike the existing linear fringe Fourier transform profilometry (LFFTP), the use of circular fringes in the proposed circular fringe Fourier transform profilometry (CFFTP) have several advantages like relatively more accurate 3D profiling of the objects at lower carrier frequencies and even at high dynamic range of the object height profile. All these aspects are presented in detail in the rest of this paper. We note that (Zhao et al., 2016) have used circular fringes with sinusoidal intensity variations along radial direction. But it is used for a different purpose of coming up with a new hardware configuration of camera and projector set-up, for obtaining a simplified calibration of 3D height and thus it does not include any algorithms or analysis for dealing with circular fringe pattern.

The rest of the paper is organized as follows. Section 2 presents the details of the existing and proposed methods. Section 3 presents a detailed evaluation of the proposed method. Finally, conclusions are presented in section 4.

2 METHODOLOGY

This section first presents the details of the existing Linear Fringe Fourier Transform Profilometry (LFFTP). It is then followed by the details of the proposed Circular Fringe Fourier Transform Profilometry (CFFTP).

2.1 Existing Linear Fringe Fourier Transform Profilometry

The sequence of steps followed for 3D profiling with LFFTP is depicted with the aid of Fig. 2 along with illustrative figures at each stage. The intensity profile of the projected pattern in LFFTP (step 1 of Fig. 2) is

$$I_L^p(x,y) = a(x,y) + b(x,y)\ \cos(2\pi f_c x + \Phi_0)$$

where f_c is the carrier or fringe frequency, (x,y) are the spatial coordinates, a represents intensity variations in the background, b represents the non-uniform reflectivity of the diffusely reflecting object and Φ_0 is the initial phase (assumed to be zero).

The intensity profile of the recorded phase modulated pattern (step 2 of Fig. 2) is

$$I_L^r(x,y) = a(x,y) + b(x,y)\ \cos(2\pi f_c x + \Phi_L(x,y)). \quad (1)$$

$\Phi_L(x,y)$ in Eq. 1 is the phase term introduced by the object height profile. In fringe projection technique, generally the underlying phase term in the phase modulated pattern contains the information about the shape of the object. Any of the fringe analysis techniques mentioned in the preceding section can be used on the modulated pattern for quantifying the underlying phase term. For ease of analysis, rewriting Eq. 1 in terms of complex exponentials using Euler formula gives

$$I_L^r(x,y) = a(x,y) + \frac{1}{2}[c(x,y)e^{j2\pi f_c x} + c^*(x,y)e^{-j2\pi f_c x}] \quad (2)$$

where $c(x,y) = b(x,y)\ e^{j\Phi_L(x,y)}$ for real $b(x,y)$, and c^* indicates conjugate of c. The desired parameter $\Phi_L(x,y)$ can be found by retrieving either $c(x,y)$ or

$c^*(x,y)$ from Eq. 2. LFFTP achieves the same by applying Fourier transform analysis. In LFFTP, the phase modulated pattern $(I_L^r(x,y))$ is first transformed to Fourier domain (step 3 of Fig. 2). Fourier domain representation of Eq. 2 is

$$\mathcal{F}\{I_L^r\} = A(f_x,f_y) + \frac{1}{2}[C(f_x - f_c, f_y) + C^*(f_x + f_c, f_y)] \quad (3)$$

where $\mathcal{F}$ represents Fourier transform. As $a(x,y)$ represents background intensity variations, the spectrum of $A(f_x,f_y)$ will be in the low frequency region. The spectral components around carrier frequency (f_c) are extracted using a bandpass filter, and is given by $\frac{1}{2}C(f_x - f_c, f_y)$. The filtered spectrum is then DC shifted (step 4 of Fig. 2), i.e., the resultant spectrum is shifted such that the dominant spectral component which was previously occurring at f_c, occurs now at zero Hertz. The result of DC shift is $\frac{1}{2}C(f_x,f_y)$.

The phase function found after the application of inverse Fourier transform on the DC shifted signal is wrapped (step 5 of Fig. 2) in the interval $[-\pi,\pi)$. On unwrapping (step 6 of Fig. 2), the result gives the 3D profile of the object of interest.

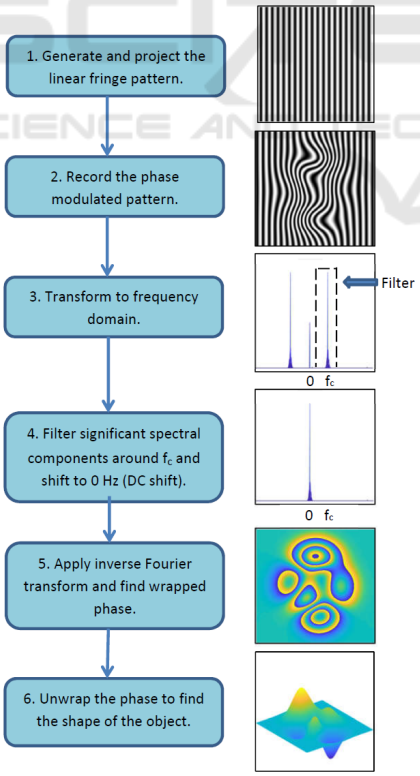

Figure 2: Block diagram illustrating the existing linear fringe Fourier transform profilometry (LFFTP) algorithm.

2.2 Proposed Circular Fringe Fourier Transform Profilometry

The sequence of steps required for 3D profiling with CFFTP is depicted with the aid of Fig. 5 along with illustrative figures at each stage. In CFFTP, the intensity profile of the circular fringe pattern projected onto the object (step 1 of Fig. 5) is

$$I_C^p(x,y) = a(x,y) + b(x,y)\cos(2\pi f_c\sqrt{x^2+y^2}). \quad (4)$$

Let $\phi^p(x,y)$ represent the argument of the cos function in the above projection equation, i.e., let $\phi^p(x,y) = 2\pi f_c\sqrt{x^2+y^2}$. Notice that $\phi^p(x,y)$ has the shape of a cone for varying values of x and y as shown in Fig. 3. The minimum value of $\phi^p(x,y)$ is zero, and it occurs at the origin.

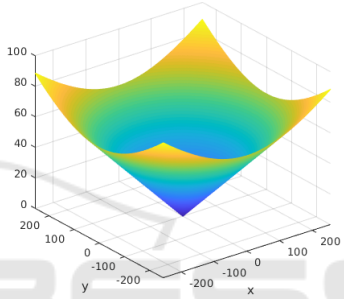

Figure 3: Phase function $(\phi^p(x,y))$ of the projected pattern. It has the shape of a cone with a minimum values of zero at origin.

When the aforementioned circular fringe pattern is projected onto the object of interest, based on the height profile of the object at that point, the pattern accordingly gets shifted in the x direction. Hence, the intensity profile of the recorded phase modulated pattern in CFFTP (step 2 of Fig. 5) is given by:

$$I_C^r(x,y) = a(x,y) + b(x,y)\cos(2\pi f_c\sqrt{(x+\delta_y(x))^2+y^2}). \quad (5)$$

Let $\phi^r(x,y)$ represent the phase function associated with the above recorded pattern, and is given by $\phi^r(x,y) = 2\pi f_c\sqrt{(x+\delta_y(x))^2+y^2}$. Note that $\phi^r(x,y)$ differs with $\phi^p(x,y)$ in terms of the modulating term $\delta_y(x)$. It can be noted that while the vortex of the projected pattern is at the origin, it is shifted by a value of $\delta_0(0)$ along the x-axis for the recorded pattern. $\delta_y(x)$ is introduced due to the object height profile, and thus it contains the information about the shape of the object. $\delta_y(x)$ can be recovered from $\phi^r(x,y)$ if f_c, x and y are known. Fringe frequency (f_c) is engineering choice and is known. The parameters x and y present in $\phi^p(x,y)$ can be used to find $\delta_y(x)$ from $\phi^r(x,y)$. Solving the phase functions $\phi^r(x,y)$ and $\phi^p(x,y)$ for $\delta_y(x)$

results in the following quadratic equation in $\delta_y(x)$:

$$\delta_y^2(x) + 2x\delta_y(x) + \frac{(\phi^p(x,y))^2 - (\phi^r(x,y))^2}{(2\pi f_c)^2} = 0 \quad (6)$$

The above quadratic equation results in two roots, and one of them corresponds to the height profile of the object. The procedure for finding out the actual root that corresponds to the object height is presented in the later part of this section.

As stated earlier, all the fringe analysis algorithms mentioned in section 1 are designed for linear fringes, and they cannot be directly applied for circular fringes. However, as illustrated in Fig. 4, circular fringes in the rectangular coordinates become linear fringes in the polar coordinates. Hence, any of the linear fringe analysis methods can be applied after transforming circular fringes into polar coordinates.

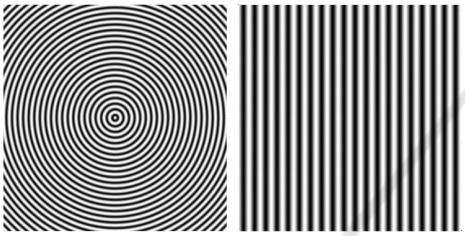

(a) Circular fringes (b) Polar equivalent of circular fringes

Figure 4: Circular fringes in Cartesian coordinates and their polar equivalents. Horizontal axis in polar representation is radius r and vertical axis is angle θ.

The proposed algorithm for retrieving the true phase of the recorded fringe pattern

Proposed Algorithm for Phase Retrieval

1. As discussed above, in order to be able to apply any of the existing linear fringe analysis algorithms, the circular fringe has to be first transformed into polar coordinates by considering the centre of the circular fringes as the origin. To this end, the centre of the recorded circular fringe is computed, and the coordinate transformation is applied. The centre of the recorded circular fringe in our experiments is computed using 'imfindcircles' function in MATLAB. Let $(x_c, 0)$ represent the centre of the recorded circular fringe. Then the equation representing the recorded fringe transformed into the polar coordinates is given by:

$$I_C^r(r', \theta) = a(r', \theta) + b(r', \theta)\ \cos(2\pi f_c r'), \quad (7)$$

where

$$r' = \sqrt{(x - x_c + \delta_y(x))^2 + y^2},$$

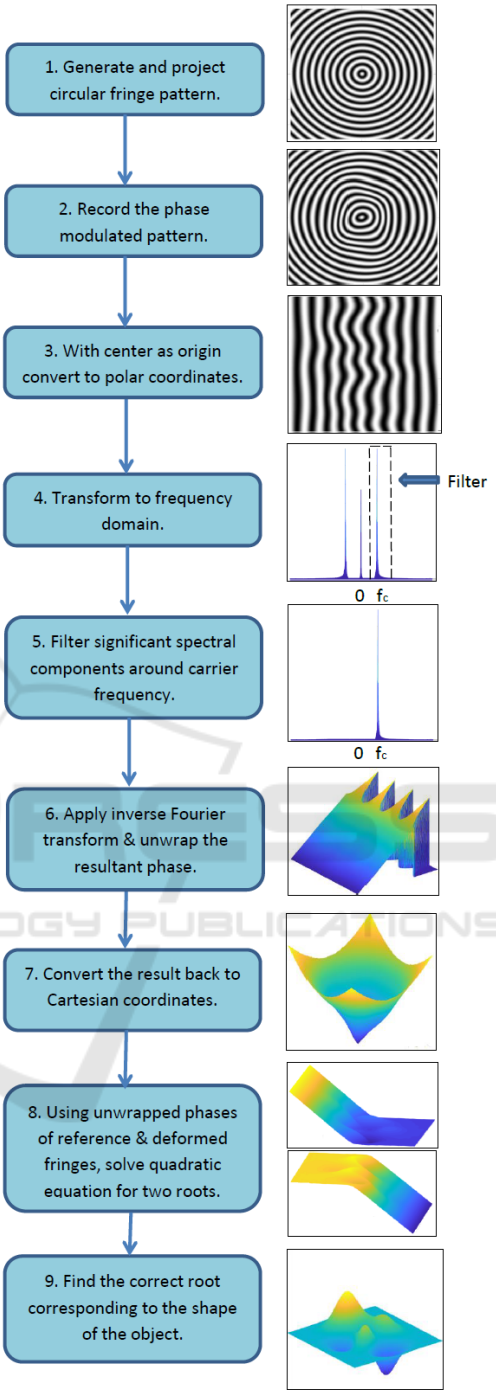

Figure 5: Block diagram illustrating the proposed circular fringe Fourier transform profilometry (CFFTP) algorithm.

$$\theta = \tan^{-1}\left(\frac{y}{(x - x_c + \delta_y(x))}\right).$$

The result of this polar coordinates transformation is illustrated in step 3 of Fig. 5.

2. Fourier transform profilometry is applied on the

fringe pattern represented by Eq. 7. The resulting frequency domain representation is given by:

$$\mathcal{F}\{I_C^r\} = A(f_{r'}, f_\theta) + \frac{1}{2}B(f_{r'} - f_c, f_\theta) + \frac{1}{2}B(f_{r'} + f_c, f_\theta). \quad (8)$$

Step 4 of Fig. 5 illustrates the resulting magnitude spectrum.

3. The spectral components around carrier frequency are extracted using a bandpass filter. The result of bandpass filtering is given by $\frac{1}{2}B(f_{r'} - f_c, f_\theta)$, and it is illustrated in step 5 of Fig. 5.

4. Inverse Fourier transform is applied on the output of the bandpass filter, and the result is given by: $\frac{1}{2}b(r', \theta)\, e^{j2\pi f_c r'}$. As discussed in section 1, the resultant phase of the above expression is wrapped into the range $[-\pi, \pi)$. It is then unwrapped using any of the phase unwrapping methods, and is illustrated in step 6 of Fig. 5.

5. The unwrapped phase is transformed back into Cartesian coordinates to get $\phi^r(x,y)$, and is illustrated in step 7 of Fig. 5.

The above mentioned algorithm can extract $\phi^p(x,y)$, $\phi^r(x,y)$, and the remaining task now is to compute $\delta_y(x)$ based on Eq. 6.

Solving the quadratic Eq. 6 for each row (y), by substituting ϕ^p and ϕ^r, gives two roots for $\delta_y(x)$ as shown in step 8 of Fig. 5. Two such roots found from Eq. 6 for one of the rows are shown in Fig. 6(a). The actual root that corresponds to the height profile of the object is obtained by imposing the following two constraints. Firstly, it is considered that the height profile is continuous over neighbourhood spatial locations. Secondly, the difference in the position of vortices of $\phi^p(x,y)$ and $\phi^r(x,y)$ is relatively nearer to the average value of the object height profile. Fig. 6(b) shows the actual root extracted from the two roots displayed in Fig. 6(a) after imposing the above constraints. Applying the same procedure for all the rows gives the actual root corresponding to the shape of the object as shown in step 9 of Fig. 5.

Finally, after the computation of $\delta_y(x)$, the actual height profile of the object is obtained using the following calibration equation (Zhang et al., 2002)

$$H(x,y) = \frac{k\,\delta_y(x)}{d - \delta_y(x)} \quad (9)$$

where k is the distance between the camera and reference plane, d is the baseline distance between the camera and projector.

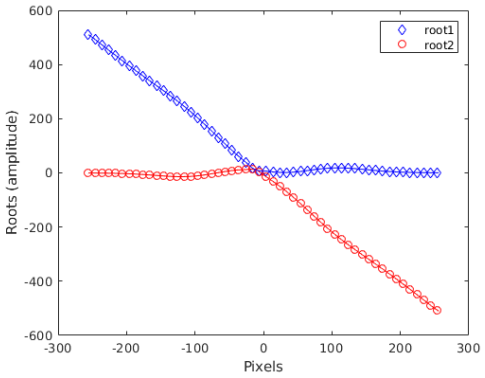

(a) Roots obtained by solving the quadratic Eq. 6.

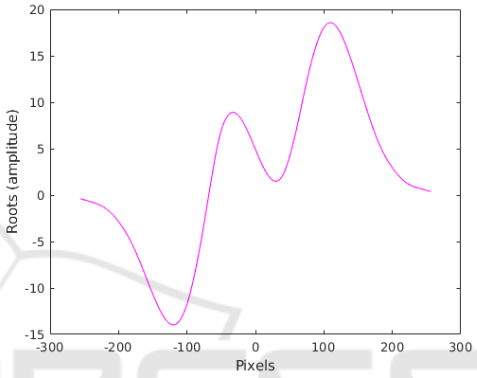

(b) Actual root extracted form the two roots.

Figure 6: Illustration of the two roots obtained by solving Eq. 6 for one of the rows, and the extracted actual root that corresponds to the height profile of the object.

3 RESULTS

In this section, we present a comparison of the results from the proposed circular fringe projection based method (CFFTP) with the results from the existing linear fringe projection based method (LFFTP). More specifically, the accuracies of the CFFTP and LFFTP methods are evaluated for varying dynamic range of the objects, and also for varying fringe frequencies.

The evaluations are performed on simulated data with varying shapes and dynamic ranges. Various shapes are generated through Gaussian Mixture Models (GMM) by randomly choosing the locations of the peaks and valleys with the help of a random number generator. Fig. 7 shows samples of such randomly generated object height profiles. While performing evaluations for varying dynamic range, those randomly generated shapes are scaled accordingly.

Fig. 8 shows the results obtained from LFFTP and CFFTP when reconstructing the height profile of the simulated object shown in Fig. 7(a). The fringe fre-

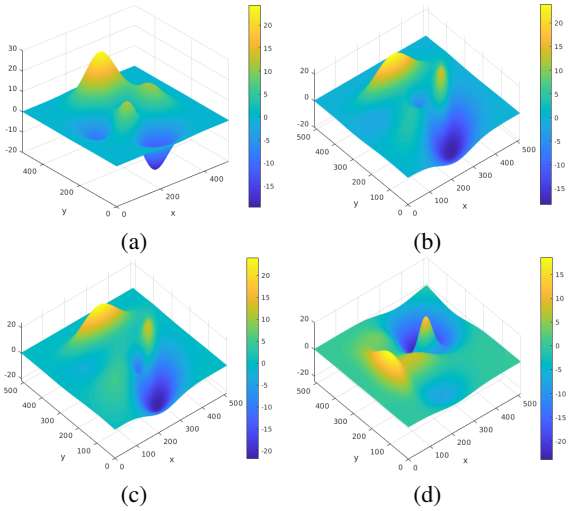

Figure 7: Sample simulated objects with arbitrary height profiles.

quency and the dynamic range values used for this particular evaluation are 20 Hz and ±24 pixels respectively. The left and the right columns of this figure present the results from the LFFTP and CFFTP respectively. First row in Fig. 8 shows the projected patterns. Second row of the same figure shows the modulated patterns in LFFTP and CFFTP. Fig. 8(e) is the magnitude spectrum of the deformed linear fringe pattern, and Fig. 8(f) is the magnitude spectrum of the deformed circular fringe pattern after transforming it into polar coordinates. It can be observed from Fig. 8(e) and Fig. 8(f) that for a given height profile of the object, the spectral variations in the magnitude spectrum of LFFTP are relatively more than that of in CFFTP. Fig. 8(g) and Fig. 8(h) show 3D profiling results obtained from LFFTP and CFFTP respectively.

In order to quantify the accuracies of the results from LFFTP and CFFTP, the difference between the ground truth and the reconstructed output from these methods are computed at each pixel. These values are normalized by dividing with the dynamic range (i.e., the difference between the maximum and minimum values of the ground truth). Fig. 8(i) and Fig. 8(j) show the resulting error plots for LFFTP and CFFTP respectively. Maximum normalized error values are found to be 0.37 for LFFTP, and 0.064 for CFFTP. Thus, the proposed CFFTP resulted in more accurate 3D reconstruction compared to the existing LFFTP.

We have also studied the effects of varying the dynamic range on the magnitude spectrums of LFFTP and CFFTP. Fig. 9 presents the magnitude spectrums of LFFTP and CFFTP for varying dynamic range. It can be observed from these results that for the proposed CFFTP, aliasing in frequency domain is starting to occur at relatively high dynamic range values than

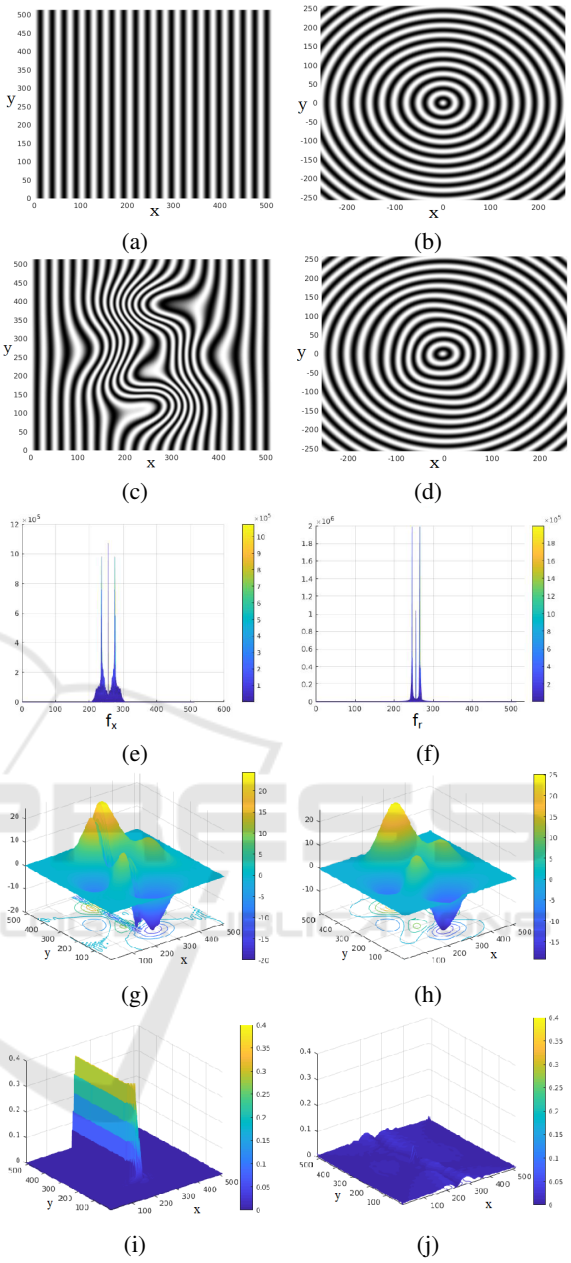

Figure 8: Simulation results from the existing LFFTP and the proposed CFFTP are presented in the first and second columns respectively. Projected fringes, deformed fringes, magnitude spectrum, reconstructed object height profiles, and normalized error values are presented in rows 1, 2, 3, 4, and 5 respectively.

that LFFTP. Because of such narrowband properties of CFFTP, it is able to more accurately reconstruct the 3D profiles of the objects having high dynamic range than LFFTP.

Fig. 10 shows the effect of varying the dynamic range on the 3D reconstruction results of LFFTP and CFFTP. For this purpose, all the height profiles shown

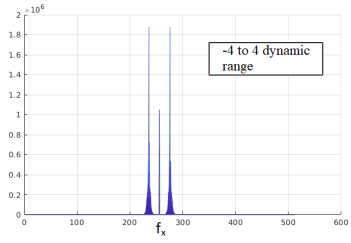

(a) LFFTP with a dynamic range of ±4.

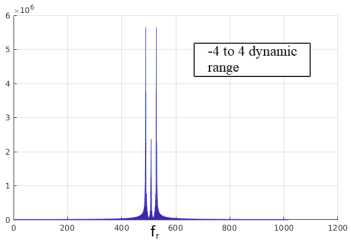

(b) CFFTP with a dynamic range of ±4.

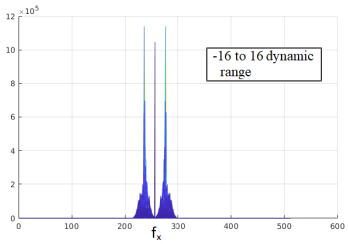

(c) LFFTP with a dynamic range of ±16.

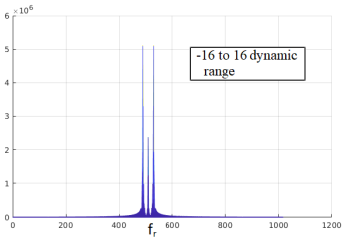

(d) CFFTP with a dynamic range of ±16.

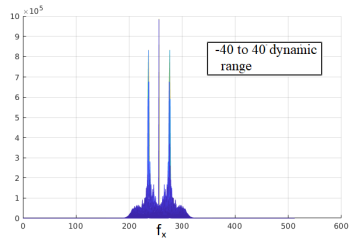

(e) LFFTP with a dynamic range of ±40.

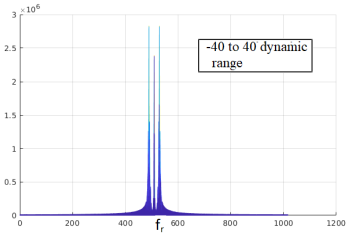

(f) CFFTP with a dynamic range of ±40.

Figure 9: Illustration of spectral changes in the magnitude spectrums of the LFFTP and the proposed CFFTP with varying dynamic range.

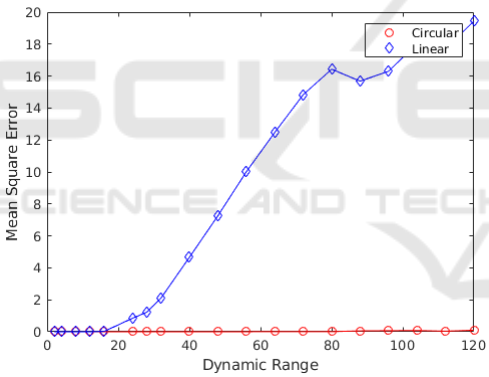

Figure 10: Plot of normalized MSE showing the comparative performance of LFFTP and CFFTP for increasing dynamic range of the object height. CFFTP has low normalized MSE at high dynamic ranges of object height for a fringe frequency of 20 Hz.

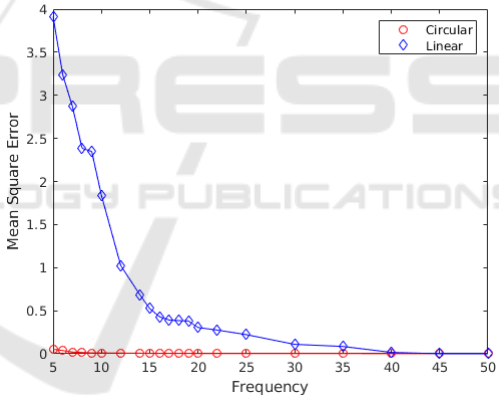

Figure 11: Plot of normalized MSE showing the comparative performance of LFFTP and CFFTP for increasing fringe frequency. CFFTP has low normalized MSE at low fringe frequency for a dynamic range of ±24.

in Fig. 7 are considered, and Mean Square Error (MSE) values presented in Fig. 10 are the averaged values computed across all the datasets. Some of the intermediate MSE values corresponding to this evaluation are presented in Table 1. Notice that if the normalized MSE value is 0.85, it means that the MSE is 85% of the dynamic range of the object height. Thus, CFFTP is found to result in significantly lower error values than the existing LFFTP, particularly at high dynamic range values. Finally, Fig. 11 shows normalized MSE values for varying fringe frequencies, for a dynamic range of ±24. Similar to the preceding experiment, MSE values are averaged across all the datasets. It can be observed that while both LFFTP and CFFTP perform equally well at high frequencies, the proposed CFFTP significantly outperforms LFFTP at low frequencies.

4 CONCLUSIONS

In this paper, we have presented a new circular fringe Fourier transform profilometry (CFFTP) method for 3D profiling of objects. Unlike the conventional linear fringes, the proposed method uses circular fringes

Table 1: Normalized MSE values in case of LFFTP and CFFTP for increasing dynamic range of object height.

Dynamic range of the object height	Normalized MSE	
	LFFTP	CFFTP
± 4	0.00	0.00
± 8	0.00	0.00
± 16	0.02	0.00
± 24	0.85	0.00
± 40	4.66	0.00
± 56	10.01	0.00
± 80	16.43	0.01
± 120	19.44	0.10
± 160	18.06	5.83

with sinusoidal intensity variations along the radial direction. A new algorithm is also proposed for retrieving the phase information from the circular fringes. The proposed CFFTP has been evaluated for varying dynamic ranges and fringe frequencies. It is found that the proposed algorithm significantly outperforms the existing LFFTP, particularly at high dynamic ranges and low fringe frequencies. In the future work, we plan to evaluate the proposed CFFTP method for the 3D profiling of the real-world objects.

REFERENCES

Asundi, A. and Wensen, Z. (1998). Fast phase-unwrapping algorithm based on a gray-scale mask and flood fill. *Applied optics*, 37(23):5416–5420.

Baldi, A. (2003). Phase unwrapping by region growing. *Applied optics*, 42(14):2498–2505.

Chen, L., Quan, C., Tay, C. J., and Fu, Y. (2005). Shape measurement using one frame projected sawtooth fringe pattern. *Optics communications*, 246(4-6):275–284.

Dias, J. M. and Leitão, J. M. (2002). The *ZπM* algorithm: a method for interferometric image reconstruction in SAR/SAS. *IEEE Transactions on Image processing*, 11(4):408–422.

Dursun, A., Özder, S., and Ecevit, F. N. (2004). Continuous wavelet transform analysis of projected fringe patterns. *Measurement Science and Technology*, 15(9):1768.

Gdeisat, M. A., Burton, D. R., and Lalor, M. J. (2006). Spatial carrier fringe pattern demodulation by use of a two-dimensional continuous wavelet transform. *Applied optics*, 45(34):8722–8732.

Goldstein, R. M., Zebker, H. A., and Werner, C. L. (1988). Satellite radar interferometry: Two-dimensional phase unwrapping. *Radio science*, 23(4):713–720.

Gorthi, S. S. and Rastogi, P. (2010). Fringe projection techniques: whither we are? *Optics and lasers in engineering*, 48(IMAC-REVIEW-2009-001):133–140.

Gutmann, B. and Weber, H. (2000). Phase unwrapping with the branch-cut method: role of phase-field direction. *Applied optics*, 39(26):4802–4816.

Iwata, K., Kusunoki, F., Moriwaki, K., Fukuda, H., and Tomii, T. (2008). Three-dimensional profiling using the fourier transform method with a hexagonal grating projection. *Applied optics*, 47(12):2103–2108.

Jia, P., Kofman, J., and English, C. (2008). Error compensation in two-step triangular-pattern phase-shifting profilometry. *Optics and Lasers in Engineering*, 46(4):311–320.

Kemao, Q. (2004). Windowed fourier transform for fringe pattern analysis. *Applied Optics*, 43(13):2695–2702.

Kemao, Q. (2007). Two-dimensional windowed fourier transform for fringe pattern analysis: principles, applications and implementations. *Optics and Lasers in Engineering*, 45(2):304–317.

Lin, J.-F. and Su, X. (1995). Two-dimensional fourier transform profilometry for the automatic measurement of three-dimensional object shapes. *Optical Engineering*, 34(11):3297–3303.

Sajan, M., Tay, C., Shang, H., and Asundi, A. (1998). Improved spatial phase detection for profilometry using a tdi imager. *Optics communications*, 150(1-6):66–70.

Servin, M., Cuevas, F. J., Malacara, D., Marroquin, J. L., and Rodriguez-Vera, R. (1999). Phase unwrapping through demodulation by use of the regularized phase-tracking technique. *Applied Optics*, 38(10):1934–1941.

Su, X. and Chen, W. (2001). Fourier transform profilometry:: a review. *Optics and lasers in Engineering*, 35(5):263–284.

Takeda, M. and Mutoh, K. (1983). Fourier transform profilometry for the automatic measurement of 3-d object shapes. *Applied optics*, 22(24):3977–3982.

Toyooka, S. and Iwaasa, Y. (1986). Automatic profilometry of 3-d diffuse objects by spatial phase detection. *Applied Optics*, 25(10):1630–1633.

Zhang, C., Huang, P. S., and Chiang, F.-P. (2002). Microscopic phase-shifting profilometry based on digital micromirror device technology. *Applied optics*, 41(28):5896–5904.

Zhang, S., Li, X., and Yau, S.-T. (2007). Multilevel quality-guided phase unwrapping algorithm for real-time three-dimensional shape reconstruction. *Applied optics*, 46(1):50–57.

Zhao, H., Zhang, C., Zhou, C., Jiang, K., and Fang, M. (2016). Circular fringe projection profilometry. *Optics letters*, 41(21):4951–4954.

Zhong, J. and Weng, J. (2004). Spatial carrier-fringe pattern analysis by means of wavelet transform: wavelet transform profilometry. *Applied optics*, 43(26):4993–4998.